Available online at www.sciencedirect.com
ScienceDirect
Journal of Catalysis 255 (2008) 313–323
JOURNAL OF CATALYSIS
www.elsevier.com/locate/jcat

The rate and selectivity of methane oxidation over $La_{0.75}Sr_{0.25}Cr_xMn_{1-x}O_{3-\delta}$ as a function of lattice oxygen stoichiometry under solid oxide fuel cell anode conditions

Michael van den Bossche, Steven McIntosh *

Department of Chemical Engineering, University of Virginia, Charlottesville, VA 22904-4741, USA

Received 25 September 2007; revised 14 February 2008; accepted 25 February 2008

Available online 20 March 2008

Abstract

Perovskite-structured $La_{0.75}Sr_{0.25}Cr_xMn_{1-x}O_{3-\delta}$ (LSCM, $x = 0$, 0.25, 0.50, 0.75, and 1) is a potential anode material for direct hydrocarbon solid oxide fuel cells (SOFCs). A pulse reactor system was used to determine the catalytic activity and selectivity of LSCM toward methane total oxidation f between 700 and 900 °C in the absence of gas-phase oxygen. This replicates the SOFC anode environment, in which oxidation occurs through reduction of the oxide lattice. Activity and selectivity were characterized as a function of lattice oxygen stoichiometry, $3 - \delta$. As $3 - \delta$ decreased, the selectivity toward total oxidation decreased for all compositions due to either a change toward partial oxidation or increased dry-reforming activity. The reaction rate and range of oxygen stoichiometry favoring total oxidation increased with increasing Mn content. This was accompanied by a decrease in both carbon formation and oxide stability. These measurements suggest that more-active catalysts are required for SOFC applications.

Keywords: Solid oxide fuel cell; SOFC; Perovskite anode; Lanthanum chromate; LSCM; Oxygen stoichiometry; Methane oxidation; Pulse reactor

1. Introduction

Solid oxide fuel cells (SOFCs) are considered one of the most promising candidates for future power generation. The primary difference between SOFCs and the commonly discussed proton-exchange membrane fuel cells (PEMFCs) is that whereas PEMFCs operate through proton transport from the fuel electrode (anode) to the air electrode (cathode), SOFCs operate through oxygen anion transport from the cathode to the anode. This difference in mechanism can allow SOFCs to operate on a wide range of fuels, including conventional petroleum, diesel, and natural gas and future bioderived hydrocarbons [1]. In addition, due to the high SOFC operating temperature (>700 °C), SOFCs can use low-cost, sulfur- and CO-tolerant transition metal catalysts. The primary challenge in realizing these direct hydrocarbon SOFCs lies in the design and development of materials and catalysts for the SOFC anode.

The operating principle behind SOFCs is illustrated in Fig. 1 [1]. Under operation, molecular oxygen is reduced to oxygen anions at the cathode, using electrons supplied from an external circuit. The generated anions then migrate through the dense, ion-conducting but electrically insulating ceramic electrolyte to the anode. Fuel oxidation occurs at the anode, and the liberated electrons flow through the external circuit to the cathode, completing the circuit and providing useful work. The ceramic electrolyte and cathode are typically dense yttria-stabilized zirconia (YSZ) and a porous $La_{1-x}Sr_xMnO_{3\pm\delta}$/YSZ composite, respectively.

Three principal anode material requirements may be derived from the SOFC operating principle: oxygen anion conductivity, electronic conductivity, and catalytic activity toward fuel oxidation. Other requirements include stability in reducing atmospheres and high temperatures (oxygen partial pressure, pO_2, as low as 10^{-24} atm; temperature >700 °C), a coefficient of thermal expansion that matches the electrolyte material, re-

* Corresponding author. Fax: +1 434 982 2658.
E-mail address: mcintosh@virginia.edu (S. McIntosh).

0021-9517/$ – see front matter
doi:10.1016/j.jcat.2008.02.021

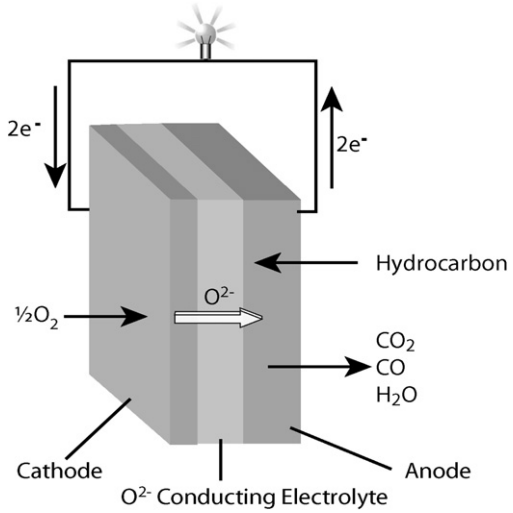

Fig. 1. Operation mechanism of a SOFC.

dox stability in case of accidental exposure to air, and resistance to sulfur poisoning. Current SOFCs use porous Ni–YSZ composite anodes in which YSZ provides ionic conductivity and Ni provides electronic conductivity and catalytic activity. Although providing high performance with hydrogen fuel, using Ni in the anode unnecessarily limits current SOFCs to hydrogen fuel or hydrocarbon fuels with a large excess of steam, because Ni catalyzes the formation of graphite with dry hydrocarbon and CO fuels [2]. In addition, the active area of these electrodes is undesirably limited to the YSZ–Ni–H_2 triple-phase points, the only regions in the electrode in which all of the anode material requirements are met [3]. Finally, Ni-based anodes are not generally redox-stable [4] and provide only limited sulfur tolerance [5].

A number of groups are investigating alternative anode materials and have demonstrated SOFC operation with a range of hydrocarbon fuels. For example, Gorte, Vohs, and coworkers have developed a Cu–CeO_2–YSZ composite anode and demonstrated its operation with a range of fuels, from methane to diesel fuel [1,6–9]. An alternative approach, aiming to create all-oxide redox-stable anodes with a reduced number of anode components, has been to develop new oxide materials that combine both conducting and catalytic functions into a single material [10–14].

Most of these proposed novel materials have a perovskite structure, general formula $ABO_{3-\delta}$. The A site is typically occupied by a lanthanide, with the B site occupied by transition metals. The perovskite structure is a focus for research, because it is able to accommodate a wide range of dopants, allowing the tailoring of the catalytic properties and ion and electron conductivity to function. The concentration of oxygen vacancies, δ in $3-\delta$, is a function of the oxidation states of the A-site and B-site cations; that is, $\delta = 0$ when the total charge on the A and B cations is 6+, balancing the charge on the three O^{2-} anions. Oxygen vacancies are formed in the lattice as the B-site cations are reduced. For a fixed composition, the lattice oxygen stoichiometry, $3-\delta$, decreases with increasing temperature and decreasing equilibrium pO_2.

Most research on perovskite anodes to date has focused on strontium titanates [15–18] and on lanthanum chromates [19–25], although lanthanum aluminates [26], vanadates [27], and ruthenates [28] have been proposed recently. $LaCrO_3$ is stable at high temperatures in reducing atmosphere [29,30] and can be doped with various transition metals. From a thermodynamic standpoint, only Mn substitution of the Cr is expected to be stable under anode operating conditions [31]; there is some debate over whether other substituents, such as Mg, Fe, Co, and Ni will be kinetically stable [31,32]. One of the most widely studied materials is $La_{0.75}Sr_{0.25}Cr_{0.50}Mn_{0.50}O_{3-\delta}$ (LSCM5050) [23,25,33,34]. Fuel cell tests on SOFCs with LSCM5050 anodes found that power densities of 0.47 and 0.2 W/cm^2 could be achieved for wet H_2 and wet CH_4, respectively, at 900 °C [23]. The diminished performance in CH_4 reflects the difference in catalytic activity of LSCM5050 toward methane and hydrogen oxidation. The focus of the present contribution is to investigate the factors governing the catalytic activity of perovskites for fuel combustion under SOFC anode conditions.

When using dry methane as a fuel, the anode material can catalyze the following reactions:

complete oxidation: $CH_4 + 4O^{2-} \rightarrow CO_2 + 2H_2O + 8e^-$

partial oxidation: $CH_4 + 3O^{2-} \rightarrow CO + 2H_2O + 6e^-$

cracking: $CH_4 + 2O^{2-} \rightarrow C + 2H_2O + 4e^-$

Methane may react further with the product water or CO_2 via steam or dry reforming, respectively:

steam reforming: $CH_4 + H_2O \rightarrow CO + 3H_2$

dry reforming: $CH_4 + CO_2 \rightarrow 2CO + 2H_2$

To realize the maximum SOFC efficiency, both in terms of fuel utilization and maximum cell potential, the anode material should selectively catalyze the complete oxidation of fuel. Cracking is especially undesirable, because it will block the active sites and ultimately lead to mechanical failure of the cell [35]. Previous catalytic studies on the LSCM system by Tao et al. [24] indicated that complete oxidation is favored at temperatures of 700–900 °C and a pO_2 of 0.1–0.7 atm. EXAFS measurements suggest that Mn is the active species, because only Mn changes oxidation state when LSCM5050 is reduced in hydrogen. This conclusion is supported by the earlier work of Yamazoe and Teraoka [36], who suggested that the oxidation activity of perovskite oxides is dictated by the B-site cation, suggesting a Mars–van Krevelen-type mechanism due to a B-site redox couple.

One primary issue with these previous studies is that the pO_2 during the measurements is many orders of magnitude greater than that in the SOFC anode [24]. There is no gas-phase oxygen at the SOFC anode; the pO_2 is set by gas-phase equilibration between fuel and oxidation products. Consequently, the oxidation state of the B-site cations will be lower, and the number of oxygen vacancies, δ, will differ significantly between the SOFC anode and the previous catalytic studies. These oxygen vacancies are analogous to the reduced oxygen reaction site in a Mars–van Krevelen mechanism. Reoxidation of the

Table 1
Fitted crystallographic parameters and BET surface areas of the studied samples

Sample	Composition	Calc. T [°C]	Space group	Lattice constant			BET [m^2/g]
				a [Å]	b [Å]	c [Å]	
LSC	$La_{0.75}Sr_{0.25}CrO_{3-\delta}$	1300	*Pnma*	5.526	5.512	7.776	0.76
LSCM7525	$La_{0.75}Sr_{0.25}Cr_{0.75}Mn_{0.25}O_{3-\delta}$	1000	$R\bar{3}c$	5.526	5.526	13.38	3.33
LSCM5050	$La_{0.75}Sr_{0.25}Cr_{0.50}Mn_{0.50}O_{3-\delta}$	1000	$R\bar{3}c$	5.526	5.526	13.40	2.42
LSCM2575	$La_{0.75}Sr_{0.25}Cr_{0.25}Mn_{0.75}O_{3-\delta}$	1000	$R\bar{3}c$	5.538	5.538	13.43	3.22
LSM	$La_{0.75}Sr_{0.25}MnO_{3-\delta}$	1000	$R\bar{3}c$	5.538	5.538	13.43	4.60

reaction site in the SOFC anode occurs via oxygen anion diffusion through the bulk ceramic from the electrolyte, not via gas-phase oxygen as in previous catalytic studies. Ultimately, the high-pO_2 environment used in previous studies will lead to an oxygen-rich perovskite lattice such that the observed activity and selectivity may not be applicable to the oxygen-lean conditions in the SOFC anode. We are developing a pulse reactor technique to determine hydrocarbon oxidation activity and selectivity as a function of lattice oxygen stoichiometry under SOFC anode conditions, where the only oxygen source is the bulk oxide catalyst. In the present study, we investigated the influence of lattice oxygen on the activity and selectivity of $La_{0.75}Sr_{0.25}Cr_{1-x}Mn_xO_{3-\delta}$ catalysts toward total oxidation of methane.

A series of catalyst powders, $x = 0$, 0.25, 0.5, 0.75, and 1 in $La_{0.75}Sr_{0.25}Cr_{1-x}Mn_xO_{3-\delta}$, were synthesized and characterized by XRD, BET, and temperature-controlled reduction of methane TPR-CH_4. The activity and selectivity toward total oxidation of methane were determined as a function of oxygen stoichiometry using a pulse reactor system in which short pulses of dry methane were interspersed with longer dwells in argon. Starting with a fully oxidized sample, each methane pulse titrated a small amount of oxygen from the sample, leading to an incremental decrease in $3 - \delta$. The initial oxygen stoichiometry was determined by thermogravimetric analysis (TGA). Repeated pulses allowed determination of the selectivity toward total oxidation as a function of lattice oxygen stoichiometry. Experiments were performed at 600, 700, 800, and 900 °C. These measurements were compared with those for a 2.7 wt% Pt surface-doped LSCM5050 sample and to the rate of hydrogen oxidation over LSCM5050. The amount of carbon formed on the powder was determined by temperature-programmed oxidation (TPO).

2. Experimental

$La_{0.75}Sr_{0.25}CrO_{3-\delta}$ (LSC), $La_{0.75}Sr_{0.25}Cr_{0.75}Mn_{0.25}O_{3-\delta}$ (LSCM7525), $La_{0.75}Sr_{0.25}Cr_{0.50}Mn_{0.50}O_{3-\delta}$ (LSCM5050), $La_{0.75}Sr_{0.25}Cr_{0.25}Mn_{0.75}O_{3-\delta}$ (LSCM2575), and $La_{0.75}Sr_{0.25}MnO_{3-\delta}$ (LSM) powders were fabricated by a sol–gel technique [37]. Aqueous solutions of La, Sr, Cr, and Mn nitrate salts (Alfa Aesar, >99.98%) were prepared, and the metal concentration was determined by complexometric titration with EDTA or by redox titration in the case of Cr [38]. These nitrate solutions were then mixed in the appropriate molar ratios with EDTA or, in the case of LSC and LSCM7525, with a mixture of EDTA and citric acid as chelating agents. Subsequent evaporation of excess water resulted in a homogeneous gel. This gel was pyrolyzed at 300 °C, and the resulting powder was calcined at 1000–1300 °C (Table 1). The powder was sieved, and the fraction between 106 and 212 μm was used for the TPR and pulsing experiments described below. LSCM5050 powder with 2.7 wt% Pt was prepared by adding 0.005 M $PtCl_4$ in 0.05 M HNO_3 solution to the LSCM5050 powder and evaporating the water. The resulting powder was heated to 450 °C to decompose the salt.

Powder X-ray diffraction patterns were recorded using Cu$K\alpha$ radiation with fixed slit width (Scintag X-Ray Diffraction XDS 2000). Diffraction patterns were recorded in the 2θ-range of 20°–65° using a 0.02° step size and a counting time of 1 min/degree. Rietveld structural refinements were carried out using the GSAS package [39]. The BET surface areas were measured (Micromeritics ASAP 2020) using N_2 as the adsorbent. Samples were degassed at 400 °C for 6 h before measurement.

The oxygen stoichiometry of the perovskite powders was determined via thermogravimetric analysis (TGA) (TA Instruments, SDT Q600 DSC/TGA). The powders were treated in air for 30 min at 1000 °C and cooled at a rate of 5 °C/min to remove surface carbonates before measurement. The sample mass, initially between 13 and 41 mg, was recorded as a function of temperature, equilibrating for 4 h at 100 °C increments between 600 and 900 °C, in both 100 ml/min N_2 and a mixture of 20 ml/min H_2 in 100 ml/min N_2 (both UHP, <2 ppm O_2). Using the level of oxygen impurity in the UHP gases, the gas-phase pO_2 in UHP N_2 was $O(10^{-6})$ atm, and in the H_2/N_2 mixture was $O(10^{-30})$ atm. The mass stabilized to within the accuracy range of the instrument during the dwells.

Temperature-programmed reduction (TPR) experiments were performed by packing 0.25 g of powder in a $\frac{1}{4}''$ i.d. quartz glass tube, held in place with quartz glass wool. The tube was sealed at both ends and heated at 10 °C/min to 900 °C, while flowing 50 ml/min of 3% H_2/N_2 for the TPR-H_2 experiments or 50 ml/min of 20 vol% CH_4/Ar for the TPR-CH_4 experiments. All gases were UHP grade (<10 ppm O_2 for CH_4, <2 ppm O_2 for the others) with the flow controlled via mass flow controllers (Omega FMA6500). The composition of the gas mixture leaving the reactor was measured using an inline mass spectrometer (Pfeiffer Vacuum, Omnistar GSD 300).

Pulse experiments were carried out using a reactor system similar to that for the TPR experiments. First, 0.25 g of powder, sieved to a size fraction of 100–200 microns, was placed in a $\frac{1}{4}''$ i.d. quartz tube and heated to 700 °C in 50 ml/min Ar.

The gas composition then changed to 20 ml/min of 10 vol% O_2/N_2 to remove surface carbonates before the pulsing experiments. The sample was subsequently cooled to 600 °C in 20 ml/min of 10 vol% O_2/N_2 before flushing for 2 h with 50 ml/min Ar. The 2-h flushing in Ar ensured that the sample oxygen stoichiometry was fully equilibrated with the O_2 present in the Ar stream, $pO_2 = 2 \times 10^{-6}$ atm, at the reaction temperature before pulsing. After 2 h, only baseline oxygen was present in the reactor effluent. The sample was then exposed to 200 6-s pulses of 20 vol% CH_4/Ar flowing at 50 ml/min. The pulses were separated by 120-s intervals of 50 ml/min Ar. Well-defined and repeatable pulses were achieved by using a 4-way computer-controlled pneumatic switching valve (Swagelok model 131SR). Both the Ar and CH_4/Ar gas streams flowed continuously, with one entering the reactor and the other vented. The reactor effluent was continually analyzed with a sampling rate of 2.2/s using an inline mass spectrometer (Pfeiffer Vacuum, Omnistar GSD300). Quantification of the gas exiting the reactor during these experiments was accomplished by calibration of the mass spectrometer signals m/e = 28 (CO) and m/e = 44 (CO_2) at 0.016–80 vol% CO or CO_2 in 20 vol% CH_4/Ar.

To calculate the amount of CO_2 produced per pulse of methane, the CO_2 baseline value, as measured before starting the pulses, was subtracted from the pulse data. The MS signal was converted to a volume fraction of CO_2 using the calibration data, and the pulses integrated to yield the total amount of CO_2. Calculation of the amount of CO was more complex, because the m/e = 28 signal is ascribed to both N_2 and CO. The contribution from trace N_2 in the CH_4 cylinder was determined using a blank reactor and averaging the m/e = 28 signal over 10 CH_4 pulses. The CO signal was corrected for CO_2 fragmentation in the MS chamber by measuring the CO signal during CO_2 calibration. The amount of CO produced was calculated by subtracting the CO baseline, measured before the pulse, and the contributions from N_2 and CO_2 fragmentation before converting to a CO volume fraction using the calibration data. The oxygen content of the samples was tracked after each pulse by subtracting the oxygen consumed to form H_2O, CO, and CO_2. Finally, volume fractions of CO_2 and CO were converted to molar flow rates, and were corrected for sample mass and BET surface area to yield normalized rates of CO_2 and CO production.

The above procedure was repeated at 700, 800, and 900 °C. The only difference was that the sample was heated to the reaction temperature where it was exposed to 20 ml/min of 10 vol% O_2/N_2 before flushing with 50 ml/min Ar. This oxidation step served to both reoxidize the sample and remove surface carbon formed during the previous pulsing experiment. The surface carbon content was quantified via analysis of the m/e = 44 signal during reoxidation. This reoxidation step was repeated after the measurements at 900 °C. Pulse experiments were also performed for the LSCM5050 sample with 10 ml/min UHP H_2 in 40 ml/min UHP Ar. A similar procedure was used.

The methane steam and dry reforming activity of the catalysts was measured by flowing appropriate reaction mixtures through a $\frac{1}{4}''$ i.d. quartz tube containing the catalyst powder sieved to the 100–200 micron size range. The product gas was analyzed using a Gas Chromatograph (SRI Instruments, 8610C) equipped with a thermal conductivity detector and Hayesep and Molecular Sieve columns. Dry reforming was performed with a sample loading of 0.10 g of catalyst, flowing a mixture of 10 vol% CO_2 and 10 vol% CH_4 in He at a total pressure of 1 atm and temperatures of 700, 750, 800, 850, and 900 °C. For steam reforming, a gas mixture of He and CH_4 was fed through a temperature-controlled water bubbler to achieve a composition of 9 vol% H_2O and 9 vol% CH_4 in He. All of the feed lines from the bubbler exit to the reactor were heated to above 150 °C to prevent water condensation. Measurements were performed at reactor temperatures of 700, 800, and 900 °C with initial sample sizes of 0.10 g of catalyst. This sample size was increased up to 0.32 g to increase the sensitivity of the measurement and enable measurement of the reaction rate at lower temperatures. But significant conversion was only measure for LSM at 800 °C and all compositions at 900 °C. In all measurements, the total gas flow rate was varied to limit the total conversion CO_2 or CH_4 to <12%.

3. Results

Recorded XRD patterns for $La_{0.75}Sr_{0.25}Cr_{1-x}Mn_xO_{3-\delta}$ (Fig. 2) were indexed on a trigonal perovskite structure, space group $R\bar{3}c$, except for LSC, which was indexed to an orthorhombic perovskite structure, space group *Pnma*. No additional phases could be discerned. Lattice cell parameters were obtained by Rietveld fitting of the data (Table 1). $R\bar{3}c$ lattice parameters increased with manganese content; *a* increased from 5.526 Å for LSCM7525 to 5.538 Å for LSM, whereas *c* varied from 13.38 Å for LSCM7525 to 13.43 Å for LSM. The specific BET surface area of the powders varied between 2.4 and 4.6 m^2/g (Table 1), except for LSC, which had a significantly lower surface area (0.76 m^2/g) due to the higher calcination temperature required to obtain a phase-pure material.

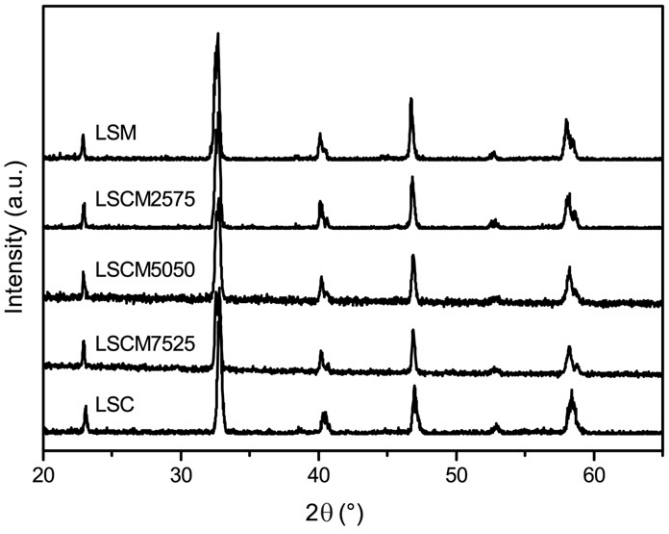

Fig. 2. X-ray diffraction patterns obtained for LSC, LSCM7525, LSCM5050, LSCM2575, and LSM powders.

Table 2
Oxygen stoichiometry of the studied samples in N_2 and 20% H_2 in N_2

T [°C]	LSC		LSCM7525		LSCM5050		LSCM2575		LSM	
	N_2	H_2/N_2	N_2	H_2/N_2	N_2	H_2/N_2	N_2	H_2/N_2	N_2	H_2/N_2
RT	3.09	3.09	3.05	3.05	2.94	2.94	2.96	2.96	2.97	2.97
600	3.06	2.89	3.00	2.79	2.90	2.74	2.93	2.72	2.92	2.47
700	3.06	2.88	2.99	2.78	2.89	2.72	2.93	2.65	2.92	2.42
800	3.05	2.88	2.98	2.76	2.89	2.68	2.92	2.57	2.91	2.40
900	2.98	2.88	2.93	2.75	2.87	2.63	2.92	2.50	2.91	2.38

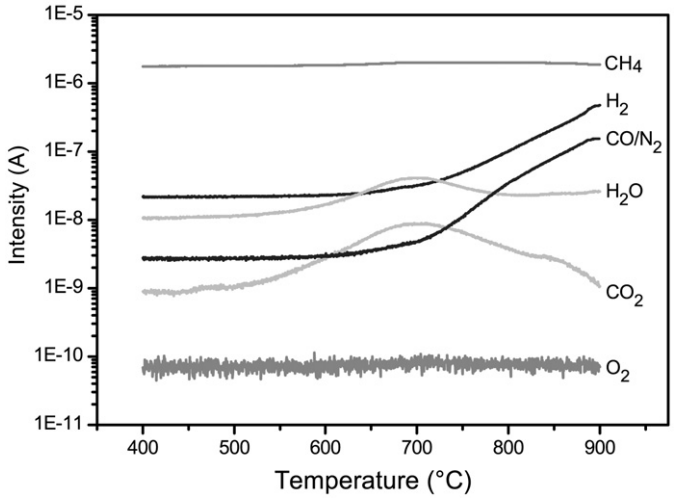

Fig. 3. TPR spectra of LSCM2575 in methane. (○) m/e = 16, (△) m/e = 2, (▲) m/e = 28, (□) m/e = 18, (■) m/e = 44, and (●) m/e = 32.

TGA experiments were performed in N_2 and H_2/N_2 on all compositions (Table 2). To calculate absolute values for the oxygen stoichiometry, it was assumed that the cation oxidation states were Cr^{3+}, La^{3+}, Mn^{2+}, and Sr^{2+} at 900 °C in 17 vol% H_2/N_2. The oxygen stoichiometry at room temperature, 600, 700, and 800 °C in H_2/N_2 were back-calculated using the loss of mass measured with the TGA. LSC and LSCM7525 had oxygen stoichiometries of 3.09 and 3.05, respectively, at room temperature, both higher than the expected value of 3.00. The room temperature oxygen stoichiometries of LSCM5050, LSCM2575, and LSM were 2.94, 2.96, and 2.97, respectively. The change in mass when heating samples in N_2 from room temperature to 900 °C was around 0.10 mol of oxygen per mol of sample; the mass of the Cr-rich samples decreased more than the Mn-rich samples in the N_2 atmosphere.

Results from TPR-CH_4 experiments are shown for LSCM2575 in Fig. 3. The mass spectrometer signals measured were m/e = 2 (attributed to H_2), 16 (CH_4, O), 18 (H_2O), 28 (N_2, CO), 32 (O_2), and 44 (CO_2). Total oxidation of methane, observed as coincidental formation of CO_2 and H_2O, started at 500 °C and reached a maximum at 660 °C. The selectivity toward total oxidation was 100% within this temperature range. Above 660 °C, partial oxidation products, CO and H_2, were observed. All compositions showed the same trend as LSCM2575, favoring total oxidation at low temperature and partial oxidation at higher temperature. One exception is LSM, which showed a second increase in CO_2 production rate starting at 800 °C. Because no gas-phase oxygen was present during these experiments, the only oxygen source for the oxidation reactions was the perovskite lattice; that is, the lattice oxygen stoichiometry, $3-\delta$, decreased with increasing temperature, due to consumption through oxidation of CH_4. As such, the question arises whether the change from total oxidation to partial oxidation is due to increasing temperature or to decreasing lattice oxygen stoichiometry.

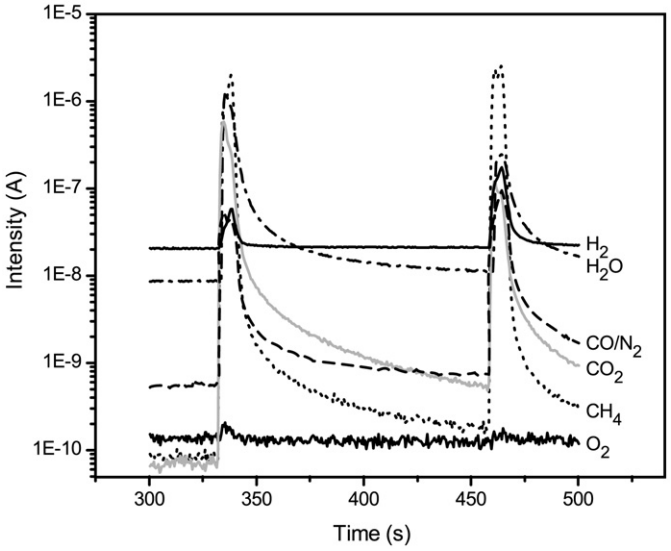

Fig. 4. Example mass spectrometer response during pulsing. At $t = 330$ and $t = 450$ s six-second methane pulses are fed to the reactor.

To address this question, a series of experiments were performed in which methane was pulsed over the sample at constant temperature. Each pulse resulted in the formation of oxidation products and a small decrease in lattice stoichiometry (maximum of 0.16 mol O per mol perovskite). Typical pulse data are shown in Fig. 4. As shown, the m/e = 16, 32, and 44 signals were negligible in Ar. H_2O and H_2 were present in background quantities, the latter due to fragmentation of H_2O in the mass spectrometer. When switching to CH_4, all signals increased except for O_2, which remained negligible. After 6 s, the CH_4 feed was switched back to Ar, and the signals decayed. Then, 120 s later, another pulse of CH_4 was fed to the reactor, and the cycle was repeated.

The instantaneous selectivity toward total oxidation of methane (i.e., the rate of CO_2 production divided by the total rate of CO and CO_2 production) is shown in Fig. 5 as a function of lattice oxygen stoichiometry at 700, 800, and 900 °C. The steps in the curves indicate the oxygen stoichiometry change for a single methane pulse. The results for 600 °C are not shown, because at this temperature the CO production rate was negligible for all compositions and could not be accurately determined. CO and CO_2 production also were measured for LSC, but due to inaccuracies in determining the very small surface area ($\sim$0.76 $m^2\,g^{-1}$) quantitative analysis of the data for LSC was not performed. The trend in selectivity with lattice oxygen stoichiometry for all temperatures and compositions was similar; selectivity toward total oxidation products decreased with decreasing lattice oxygen stoichiometry. For example, at 900 °C, LSCM7525 was a total oxidation catalyst in the oxygen stoi-

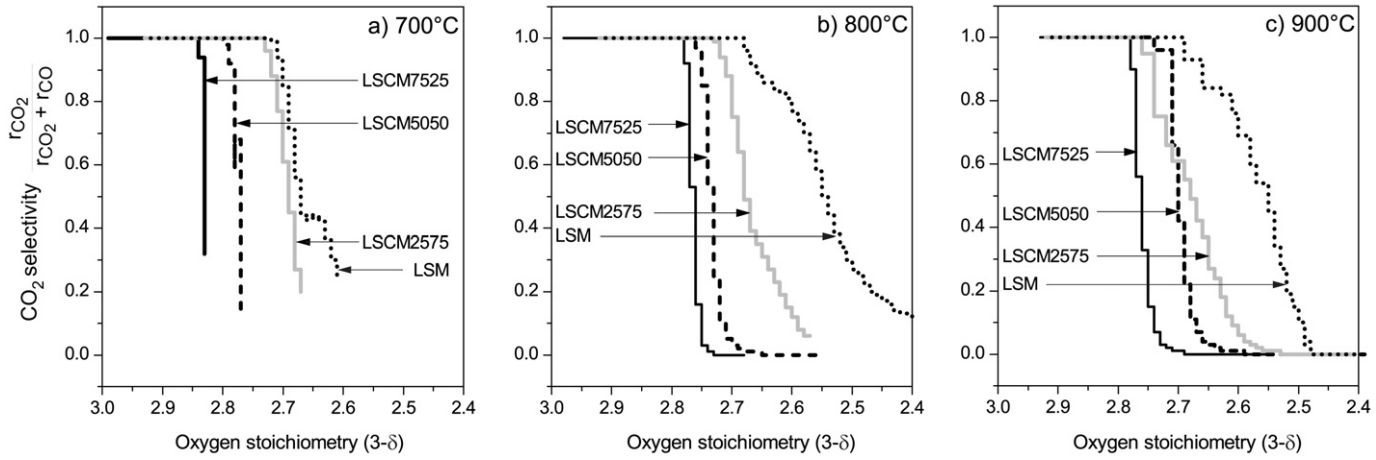

Fig. 5. Selectivity towards total oxidation of methane ($pCO_2/pCO_2 + pCO$) at (a) 700, (b) 800, and (c) 900 °C. The thick solid line is LSCM7525, solid line is LSCM5050, dashed line is LSCM2575 and dotted line is LSM.

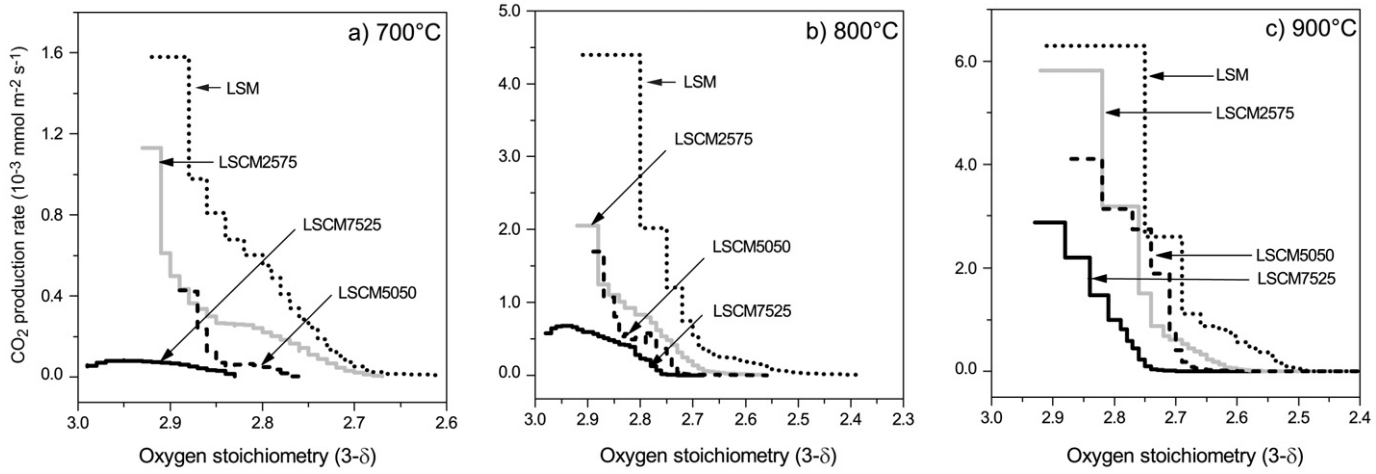

Fig. 6. CO_2 production rates at (a) 700, (b) 800, and (c) 900 °C. Thick solid line is LSCM7525, solid line is LSCM5050, dashed line is LSCM2575 and dotted line is LSM.

chiometry range 2.93–2.79. Only trace CO attributable to CO_2 fragmentation in the MS chamber, was observed over this range of oxygen stoichiometry. The selectivity then declined sharply between $3-\delta = 2.79$ and 2.72. Below $3-\delta = 2.72$, only partial oxidation products were observed until the sample equilibrated with the trace oxygen in the methane pulse and reaction ceased at $3-\delta = 2.59$. As the Mn content in the perovskite increased, the range of stoichiometry correlated to the production of total oxidation products increased; for example, CO_2 production was significant above $3-\delta = 2.68$ for LSCM2575, compared with $3-\delta = 2.76$ for LSCM7525 at 800 °C.

The surface area-normalized rates of CO_2 and CO production are shown in Figs. 6 and 7, respectively. In general, the rate of methane oxidation at a given lattice oxygen stoichiometry increased with increasing Mn content in the perovskite; for example, at $3-\delta = 2.80$ and 800 °C, the rate of CO_2 production increased in the order LSCM7525 $= 2.5 \times 10^{-4}$ > LSCM5050 $= 5.2 \times 10^{-4}$ > LSCM2575 $= 9.26 \times 10^{-4}$ > LSM $= 4.4 \times 10^{-3}$ mmol $CO_2\,m^{-2}\,s^{-1}$. As the oxygen stoichiometry decreased, the rate of CO_2 production decreased until it reached the limit of detection. As may be expected, the rate of CO_2 production increased with temperature; therefore, the highest production rate was measured as 6.3×10^{-3} mmol $m^{-2}\,s^{-1}$, for LSM at 900 °C and an oxygen stoichiometry of 2.91. CO production followed the same trend in temperature but an inverse trend with oxygen stoichiometry. The CO production rate increased once the oxygen stoichiometry dropped below a threshold value, and then peaked before decreasing below the detection limits as the sample equilibrated and reaction stopped; for example, CO production started at $3-\delta = 2.76$ for LSCM5050 at 800 °C, peaked at 5.81×10^{-4} mmol CO $m^{-2}\,s^{-1}$ at $3-\delta = 2.59$, and ceased at $3-\delta = 2.56$. At all temperatures, increased Mn content in the perovskite led to an increased rate of CO_2 production at a given oxygen stoichiometry. At the higher measurement temperatures, LSCM5050 and LSCM7525 clearly produced significantly more CO than the other two compositions; at 900 °C, the maximum CO production rates for LSCM7525 and LSCM5050 were 9.98×10^{-4} and 1.25×10^{-3} mmol CO $m^{-2}\,s^{-1}$, respectively, compared with

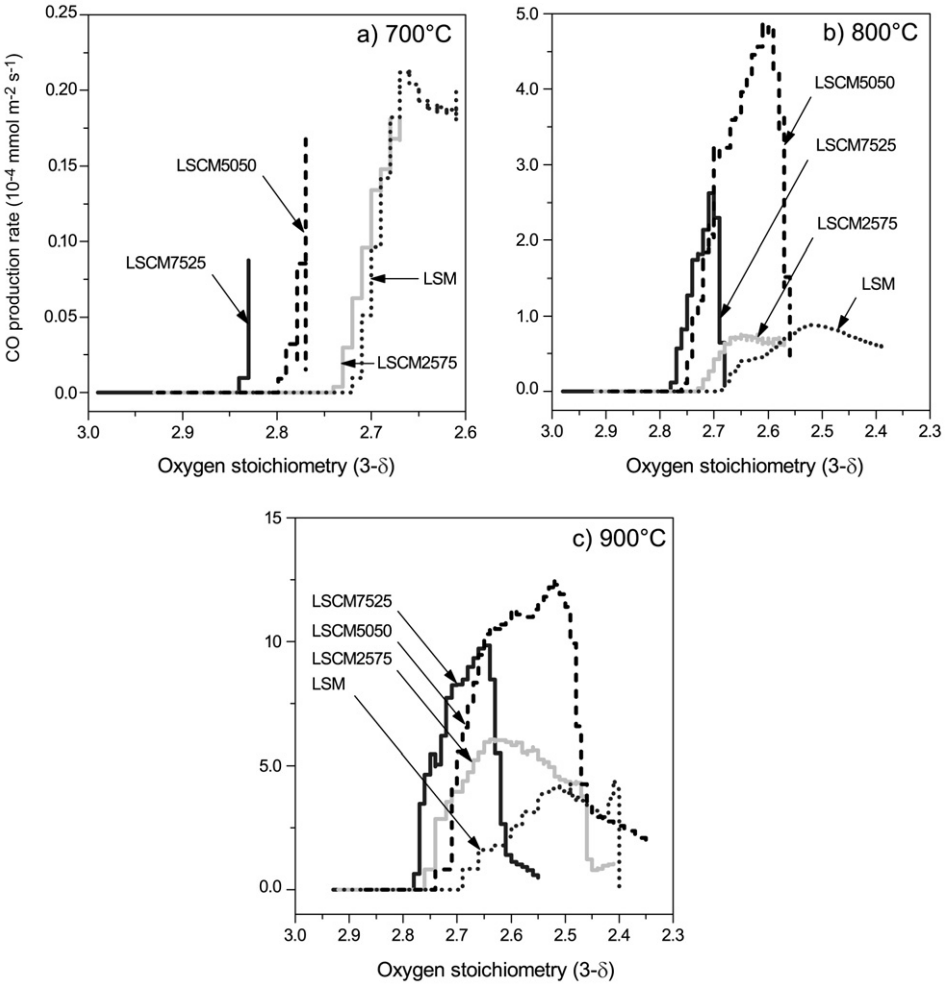

Fig. 7. CO production rates at (a) 700, (b) 800, and (c) 900 °C. The thick solid line is LSCM7525, solid line is LSCM5050, dashed line is LSCM2575 and dotted line is LSM.

6.1×10^{-4} and 4.4×10^{-4} mmol CO m^{-2} s^{-1} for LSCM2575 and LSM.

The rate of hydrogen consumption over LSCM5050 was measured using an identical pulse procedure to allow comparison with the methane combustion rate. At 700 °C, the initial reaction rate with hydrogen was 28×10^{-3} mmol m^{-2} s^{-1} of lattice oxygen. All of the hydrogen fuel was consumed by the reaction for the first few pulses, indicating that the surface reaction rate for hydrogen could be higher. The rate of hydrogen consumption decreased with decreasing oxygen stoichiometry. The rate of hydrogen consumption during the first pulse did not vary significantly with temperature, further indicating that the reaction had a limited hydrogen supply under these conditions. In comparison, for LSCM5050 with methane, reaction rates during the first pulse were 1.7×10^{-3}, 6.8×10^{-3}, and 16×10^{-3} mmol m^{-2} s^{-1} of oxygen at 700, 800, and 900 °C, respectively.

The rate of methane oxidation increased considerably with the addition of 2.7 wt% Pt to the surface of LSCM5050. At 600 and 700 °C, reaction rates were increased by a factor of 29 and 6.7 respectively, indicating that the reaction was surface-controlled. At 800 °C, the reaction rate was enhanced slightly, by a factor of 1.7. Rates at 900 °C were nearly the same, indicating that oxygen supply to the surface could be limiting at this temperature. In addition, it was found that significant CO_2 production for the platinum containing powder started at temperatures as low as 400 °C, whereas without platinum, CO_2 production was not significant below 600 °C. The selectivity toward total oxidation products as a function of oxygen stoichiometry did not change significantly with the addition of Pt. As with the undoped samples, there was a change in selectivity to partial oxidation products with decreasing lattice oxygen stoichiometry. The trend in selectivity was almost identical to that shown for undoped LSCM5050 in Fig. 5.

When interpreting this change in selectivity, we must consider the difficulty in determining whether true partial oxidation is occurring. The total oxidation products, CO_2 and H_2O, may undergo subsequent dry- or steam-reforming reactions with methane [40], resulting in the measured CO (m/e = 28) signal. To investigate this possibility, the rates of dry and steam reforming over the catalysts were measured. Fig. 8 shows the measured rates of CO production by methane dry reforming as a function of temperature for each catalyst. The feed composition was 10/10/80 vol% of CO_2/CH_4/He at a total pressure

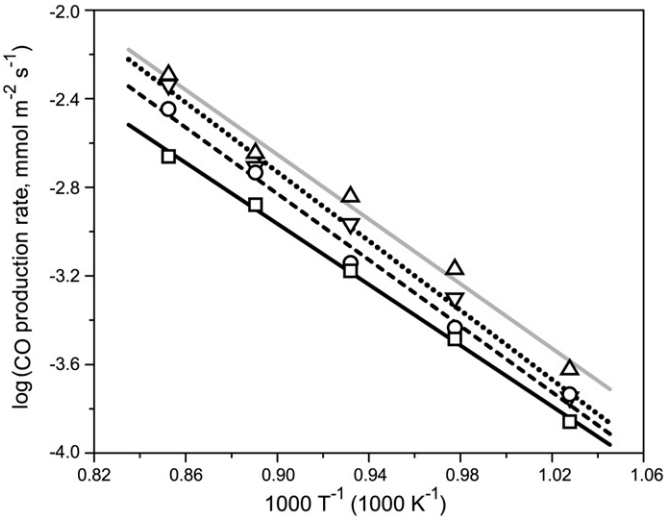

Fig. 8. CO production rate as a function of temperature for LSCM7525 (□; solid black line), LSCM5050 (○; dashed black line), LSCM2575 (△; solid gray line) and LSM (▽; dotted black line) for a 10/10/80 CO_2/CH_4/He feed at a total pressure of 1 atm. The symbol size represents the error range of the measurement.

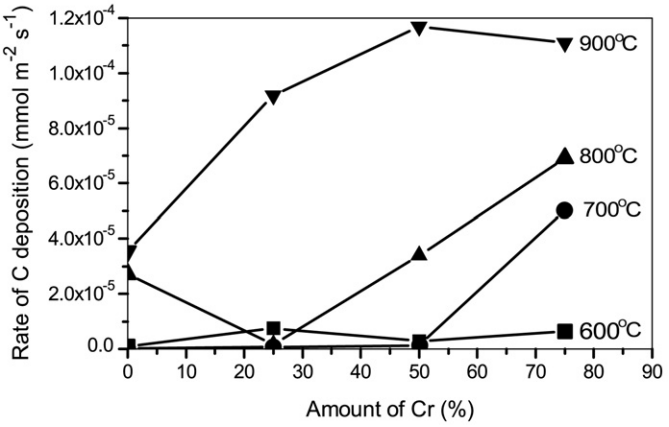

Fig. 9. Rate of carbon deposition as a function of chromium content at (■) = 600 °C, (●) = 700 °C, (▲) = 800 °C, and (▼) = 900 °C.

of 1 atm. As with the trend in CH_4 total oxidation activity measured for the pulse experiments (Fig. 6), the rate of CO production increased with increasing Mn content in the catalyst. The exceptions to this were the measured rates for LSM, which were below those of LSCM2575. This may be due to the decreased stability of the perovskite oxide structure with increasing Mn content under these severely reducing conditions. This was not observed in the pulse reactor case, because those samples were not exposed to these reducing conditions for such long periods. The measured activation energies were 131 ± 3 kJ mol^{-1} for LSCM7525, 142 ± 3 kJ mol^{-1} for LSCM5050, 143 ± 3 kJ mol^{-1} for LSCM2575, and 152 ± 3 kJ mol^{-1} for LSM. These activation energies are similar to those observed for dry reforming over other oxides such as CeO_2 [41], but significantly higher than those reported for supported metal catalysts [42].

The rates of steam reforming were significantly lower than those measured for dry reforming. No conversion of reactants was observed for any of the catalysts with a 9/9/82 vol% of H_2O/CH_4/He at a total pressure of 1 atm below 800 °C. At 800 °C, significant rates were observed only for LSM, for which the CO production rate was 2.67×10^{-4} mmol m^{-2} s^{-1}. At 900 °C, the measured CO production rates were 1.42×10^{-4}, 3.54×10^{-4}, and 3.86×10^{-4} mmol m^{-2} s^{-1}; the standard deviation in these reported rates was $\pm 1 \times 10^{-6}$ mmol m^{-2} s^{-1}.

After the pulsing experiments, samples were reoxidized while measuring the CO_2 (m/e = 44) release. The amount of CO_2 produced was calculated using a separate calibration of CO_2 performed in a 10 vol% O_2 in N_2 mixture and was related to the amount of carbon deposited on the sample during the pulsing experiment. Rates of carbon deposition for the samples at different temperatures are shown in Fig. 9. In general, the more chromium in the composition, the more carbon is deposited on the sample. Carbon deposition also depended strongly on temperature; at 600 and 700 °C, carbon deposition was almost negligible; at 900 °C, carbon deposition increased to 1.2×10^{-4} mmol m^{-2} s^{-1} for LSCM5050.

4. Discussion

The XRD patterns showed that all compositions were phase-pure perovskites. Manganese-containing compositions could be fitted on an $R\bar{3}c$ cell, in accordance with the literature [43,44]. Strontium-doped lanthanum chromate has been reported to have either a rhombohedral $R\bar{3}c$ cell [45] or an orthorhombic *Pnma* cell [46]. The orthorhombic phase was observed after sintering at 1200 °C, whereas the rhombohedral cell was reported at 1550 °C. Our LSC sample was sintered at 1300 °C; the recorded XRD pattern lacked the splitting of peaks at $2\theta = 42°$ and 58° that would be expected for a rhombohedral cell, thus indicating that the structure was orthorhombic *Pnma*. BET surface areas were found to be comparable with values for similar materials sintered at such high temperatures [20]. This low surface area is undesirable for catalysis, however; high-temperature sintering is needed to produce a phase-pure, homogeneous material and to manufacture SOFCs. The loss of catalytically active surface area must be balanced with the other demands placed on fuel cell materials, including electronic conductivity, redox stability, and compatibility with the electrolyte materials.

TPR measurements using methane showed high selectivity toward total oxidation at relatively low temperatures (500–700 °C) for all of the LSCM materials. At higher temperatures, the selectivity decreased, with a shift toward partial oxidation. The exception to this was LSM, which demonstrated an additional CO_2 production peak at 800 °C. An analogous hydrogen consumption peak was observed for LSM during hydrogen TPR experiments. XRD measurements of LSM after exposure to methane at 900 °C confirmed that LSM was not stable under these conditions, indicating that this high-temperature CO_2 peak or hydrogen consumption may be associated with decomposition of the perovskite structure. Other samples showed no additional peaks in TPR measurements with either hydrogen or methane. The XRD data confirmed that after exposure to methane at 900 °C, LSCM7525 and LSCM5050 remained pure

perovskites, but underwent a phase change from rhombohedral to orthorhombic. This effect also was reported by Zha et al. [47] for treatment in hydrogen at 1200 °C. LSCM2575 remained in the orthorhombic perovskite structure, but a small amount of an additional phase was detected. This additional phase could not be indexed to a simple Sr, La, or Mn oxide.

Although these TPR measurements are representative of the low pO_2 atmosphere in the SOFC anode, there is significant ambiguity when interpreting them. As the TPR measurements proceeded, the temperature was increased and more oxygen was consumed from the oxide lattice, reducing the oxygen stoichiometry, $3-\delta$. As such, it remains unclear whether the selectivity change was due to the change in temperature or to the change in oxygen stoichiometry. One approach to differentiating the two effects is to measure the CO_2 and CO production as a function of time at constant temperature and relating the product distribution to the oxygen content of the catalyst, because the latter will decrease as the oxidation of methane proceeds over time. The primary problem with this approach is the solid-state transport step required for oxygen to diffuse from the oxygen-rich center of the oxide particle to the surface. Continuously feeding methane over the sample would soon deplete surface oxygen, which then must be replenished by oxygen diffusion from the particle center. This leads to a risk of measuring the rate of the oxygen transport step in the bulk rather than the rate of the surface reaction. To overcome this limitation, a pulse reactor approach was chosen. In this approach, each pulse of methane consumes the lattice oxygen close to the particle surface (maximum of 0.16 mol O per mol perovskite), which is then replenished from the relatively oxygen-rich core by solid-state diffusion under the argon atmosphere between pulses. In this way, we could ensure that the measured rate was the actual rate of the surface reaction. Variation of the inert dwell time did not lead to a change in the measured reaction rate, confirming that the surface was fully equilibrated before the methane pulse. To ensure that the catalyst powder would not reoxidize by scavenging oxygen during this inert dwell, we used high-purity Ar. Calculations on the duration of the experiment and the oxygen concentration in argon demonstrated that per dwell period, the oxide lattice could scavenge at most 7×10^{-6} mol of O per mol of perovskite.

Comparison of the rates of hydrogen and methane combustion under otherwise identical experimental conditions for LSCM5050 indicates that the measured rate for methane was neither gas-phase (methane) nor solid-state (oxygen) diffusion-limited. The diffusion-limited rate for oxygen consumption by hydrogen was 28×10^{-3} mmol m^{-2} s^{-1} of lattice oxygen. This is significantly higher than all of the rates measured during the methane experiments, with the exception of the initial pulse with methane at 900 °C over LSM, which was 25×10^{-3} mmol m^{-2} s^{-1} of lattice oxygen. In addition, this single pulse consumed almost 100% of the methane fed; this represents the maximum consumption for the initial pulse over the fully oxidized sample. Subsequent pulses consumed 44% and 19% of the methane fed. Methane consumption was <10% for each subsequent pulse and for other compositions.

Further confirmation that we were measuring the surface reaction rate comes from our data for the LSCM5050 catalyst with the addition of 2 wt% platinum. Platinum is an active catalyst for oxidation of hydrocarbon fuels. As discussed earlier, the measured reaction rates were greatly enhanced by the added platinum, up to a factor of 29 at 600 °C.

The observed trend in selectivity from total oxidation to partial oxidation with decreasing lattice oxygen stoichiometry has not been reported before. One cause of the change in selectivity could be the observed change in structure from rhombohedral $R\bar{3}c$ to orthorhombic *Pnma* for LSCM7525 and LSCM5050. This is unlikely, however, because all of the materials showed the same trend in selectivity.

LSCM5050 has been previously reported to be a total oxidation catalyst, even in methane-rich CH_4/O_2 gas mixtures. Tao et al. [24] found that at 700 °C, the selectivity toward CO_2 approached 100% for gas-phase oxygen concentrations ranging from 10 to 70%. At 900 °C, CO_2 selectivity increased overall from 70% CO_2 production at 10% oxygen to 100% CO_2 production at 70% oxygen. At such high pO_2, we would anticipate an oxygen-rich lattice with relatively few oxygen vacancies ($3-\delta$ close to 3). As such, the observed selectivity toward total oxidation was consistent with our results at high oxygen stoichiometry (Fig. 5). Indeed, we observed 70% selectivity toward CO_2 at an oxygen stoichiometry of 2.71 on LSCM5050 at 900 °C; however, the conditions in the reducing environment of the SOFC anode were significantly different, with an equilibrium gas-phase pO_2 as low as 10^{-20} atm. As such, the oxygen stoichiometry of the catalyst in the anode will be closer to the equilibrium values in H_2/N_2 measured by TGA (Table 1). Consequently, we can expect LSCM-based catalysts to (undesirably) favor partial oxidation under SOFC anode conditions. This is in agreement with extrapolation of Tao et al.'s [24] selectivity data at 900 °C, which suggests that for gas-phase oxygen (<10%), partial oxidation would be favored.

The observed increase in catalytic activity with increasing Mn supports the suggestion made earlier that the active reaction site is associated with Mn on the B-site of the perovskite. It also supports a MVK-type mechanism, because Mn can be expected to be the most redox active species in $La_{0.75}Sr_{0.25}Cr_xMn_{1-x}O_{3-\delta}$ under these conditions. Methane adsorbed on the surface of the LSCM is oxidized through reduction of the B-site cation. This surface reaction site is then reoxidized by lattice oxygen diffusing from the relatively oxygen-rich core of the catalyst particle.

The measured decrease in selectivity toward total oxidation with decreasing oxygen lattice stoichiometry may be related to the availability of oxidized reaction sites. As the oxygen stoichiometry decreases, the fraction of surface reaction sites in the reduced state increases, decreasing the oxygen available for reaction and favoring partial oxidation of CH_4. An alternative to this single-step partial oxidation mechanism to form CO is a two-step mechanism in which CH_4 first undergoes total oxidation to CO_2 and H_2O, followed by a CH_4 dry-reforming step to form CO and H_2. Note that we observed no reforming or partial oxidation products at high oxygen stoichiometry, where the CO_2 partial pressure was highest. As such, a two-step mech-

anism requires that the fully oxidized catalyst be selective for total oxidation, with the reduced catalyst active for both total oxidation and dry reforming. The feasibility of such a two-step mechanism is supported by the steady-state rates of CH_4 dry reforming detailed in Fig. 8. The rates of CO production were sufficiently high to account for all of the CO measured at low oxygen stoichiometry during the pulse experiments (Fig. 7). The perovskite lattice had a low oxygen stoichiometry during these steady-state measurements due to the highly reducing gas atmosphere. The rates of steam reforming were too low to account for the observed CO production rate.

As is well documented in the literature [40], separating these two possible mechanisms is very difficult, and reaching a definitive conclusion will require significant further study. In the context of the SOFC anode, the production of CO, whether by partial oxidation or dry reforming, is undesirable. CO exiting the SOFC in the exhaust stream represents a loss of potential fuel.

In addition to the oxidation state of the lattice, we must consider the driving force for the oxidation reaction. With no oxygen fed to the reactor, all of the oxygen for CH_4 oxidation reaction in both our experiments and the SOFC anode must be supplied from the oxide lattice. As the lattice oxygen stoichiometry approached equilibrium with the gas phase, the driving force for total oxidation decreased, enabling either partial oxidation or dry-reforming reactions. Irrespective of the mechanism of CO formation, the concept of increased CO_2 production at high oxidation as a driving force is supported by the increased range of oxygen stoichiometry, which favors total oxidation with increasing Mn content (Fig. 5). As shown in Table 1, the equilibrium oxygen stoichiometry under a highly reducing atmosphere decreased with increasing concentration of the reducible Mn cation. The difference between the current oxygen stoichiometry and the equilibrium value was the driving force for further reduction of the oxide through oxidation of methane; therefore, at a fixed oxygen stoichiometry, the driving force for reaction increased with increasing Mn content. We suggest that this increased driving force led to increased formation of total oxidation products. This concept is further supported by the observation that on surface doping with an active total oxidation catalyst (Pt), the reaction selectivity demonstrated the same trend in perovskite lattice oxygen stoichiometry as the undoped sample. This further demonstrated that selectivity is determined by the driving force for reduction of the underlying perovskite lattice. An alternative explanation is that both Cr and Mn cations are active for the oxidation reaction, with Mn favoring total oxidation; however, this is in contradiction with the observed increase in activity with increasing Mn content, the selectivity toward total oxidation observed at high oxygen lattice stoichiometry for materials with high Cr content, and the data from the Pt-doped sample. Further work is needed to fully explore this concept and gain insight into the influence of mixed cations on the B-site.

One implication of the observed change in activity and selectivity as a function of oxygen stoichiometry is that the catalytic function of the LSCM materials will depend on the rate of oxygen supply to the reaction site—that is, the ionic conductivity of the catalyst material. If oxygen supply is fast relative to the surface reaction rate, then the reaction sites will be replenished with oxygen quickly enough to keep the lattice oxygen stoichiometry high and favor total oxidation. If the ionic conductivity is low, then the oxygen stoichiometry could decrease sufficiently to shift the selectivity toward the unwanted partial oxidation reaction. McIntosh et al. [8] reported a change in fuel cell reaction selectivity from partial to total oxidation on increasing the rate of oxygen supply by increasing SOFC current density; we are currently working to probe this link for LSCM-based anodes. Although increased Mn content favors total oxidation and decreases carbon deposition, it also decreases the stability of the perovskite structure under reducing conditions. These considerations must be balanced in SOFC development.

Finally, to assess the potential of these materials for use in the SOFC anode, we compared the CO_2 reaction rate on LSCM5050 with the rate required to attain an SOFC power density of 1.0 W/cm^2 at 0.5 V. The required rate is 25.9 mmol $CO_2\, m_{SOFC}^{-2}\, s^{-1}$. The highest reaction rate attained experimentally on LSCM5050 was 4.11×10^{-3} mmol $CO_2\, m_{catalyst}^{-2}\, s^{-1}$ at 900 °C, requiring an active anode surface area of 6302 $m_{catalyst}^2\, m_{SOFC}^{-2}$, or 1.5 kg of active catalyst per square meter of fuel cell. Using a density from XRD of 6.397 $g\, cm^{-3}$, this represents a dense layer 200 μm thick. This would be much thicker when incorporating the required porosity. By analogy with the SOFC cathode, we may anticipate the utilization region to extend only O(20) μm from the electrolyte interface [48]. As such, the specific activity of these materials does not appear to be sufficient. We must work to either develop fabrication techniques to increase the surface area of these materials or increase their specific activity through the perovskite composition or surface doping of more active materials.

5. Conclusion

XRD pure $La_{0.75}Sr_{0.25}Cr_xMn_{1-x}O_{3-\delta}$ ($x = 0$, 0.25, 0.50, 0.75, and 1) was synthesized using a sol–gel technique. During the TPR measurements in methane, the main oxidation product was found to change from carbon dioxide to carbon monoxide with increasing temperature. Pulse reactor studies revealed that the catalytic activity and selectivity toward total oxidation of methane for these materials decreased with decreasing lattice oxygen stoichiometry, $3 - \delta$. For all compositions and for temperatures above 700 °C, the selectivity was observed to change from 100% toward total oxidation at high oxygen stoichiometry to 100% toward partial oxidation at low oxygen stoichiometry. Measured rates of dry reforming suggest that the partial oxidation products were formed either from a single-step partial oxidation reaction or by a two-step process with total oxidation followed by dry reforming. Both the surface area-specific rate of reaction and the range of oxygen stoichiometry favoring total oxidation increased with increasing Mn content in the lattice. The measured rates of reaction were insufficient for high-performance SOFC, indicating the need for further improvements in catalytic activity of these novel oxides.

Acknowledgments

This work was supported by the National Science Foundation under the Faculty Early Career Development Program (CAREER) Grant CBET-0643931, with additional support from the American Chemical Society, Petroleum Research Fund under Grant PRF 45844-G10.

References

[1] S. McIntosh, R.J. Gorte, Chem. Rev. 104 (2004) 4845–4865.
[2] M.L. Toebes, J.H. Bitter, A.J. van Dillen, K.P. de Jong, Catal. Today 76 (2002) 33–42.
[3] M. Mogensen, S. Skaarup, Solid State Ionics 86 (8) (1996) 1151–1160.
[4] D. Sarantaridis, A. Atkinson, Fuel Cells 7 (2007) 246–258.
[5] Y. Matsuzaki, I. Yasuda, Solid State Ionics 132 (2000) 261–269.
[6] S. McIntosh, J.M. Vohs, R.J. Gorte, J. Electrochem. Soc. 150 (2003) A1305–A1312.
[7] S. McIntosh, J.M. Vohs, R.J. Gorte, J. Electrochem. Soc. 150 (2003) A470–A476.
[8] S. McIntosh, J.M. Vohs, R.J. Gorte, Electrochim. Acta 47 (2002) 3815–3821.
[9] H. Kim, S. Park, J.M. Vohs, R.J. Gorte, J. Electrochem. Soc. 148 (2001) A693–A695.
[10] A. Atkinson, S. Barnett, R.J. Gorte, J.T.S. Irvine, A.J. McEvoy, M. Mogensen, S.C. Singhal, J. Vohs, Nat. Mater. 3 (2004) 17–27.
[11] S.P. Jiang, S.H. Chan, J. Mater. Sci. 39 (2004) 4405.
[12] J.W. Fergus, Solid State Ionics 177 (2006) 1529–1541.
[13] V.V. Kharton, A.A. Yaremchenko, A.A. Valente, V.A. Sobyanin, V.D. Belyaev, G.L. Semin, S.A. Veniaminov, E.V. Tsipis, A.L. Shaula, J.R. Frade, J. Rocha, Solid State Ionics 176 (2005) 781–791.
[14] S.W. Tao, J.T.S. Irvine, Chem. Rec. 4 (2004) 83–95.
[15] Q.X. Fu, F. Tietz, D. Stover, J. Electrochem. Soc. 153 (2006) D74–D83.
[16] D.P. Fagg, V.V. Kharton, A.V. Kovalevsky, A.P. Viskup, E.N. Naumovich, J.R. Frade, J. Eur. Ceram. Soc. 21 (2001) 1831–1835.
[17] O.A. Marina, N.L. Canfield, J.W. Stevenson, Solid State Ionics 149 (2002) 21–28.
[18] X.L. Huang, H.L. Zhao, W. Shen, W.H. Qiu, W.J. Wu, J. Phys. Chem. Solids 67 (2006) 2609–2613.
[19] S.W. Tao, J.T.S. Irvine, Chem. Mater. 16 (2004) 4116–4121.
[20] J. Sfeir, P.A. Buffat, P. Mockli, N. Xanthopoulos, R. Vasquez, H.J. Mathieu, J. Van Herle, K.R. Thampi, J. Catal. 202 (2001) 229–244.
[21] J. Liu, B.D. Madsen, Z.Q. Ji, S.A. Barnett, Electrochem. Solid State Lett. 5 (2002) A122–A124.
[22] S.W. Tao, J.T.S. Irvine, J. Electrochem. Soc. 151 (2004) A252–A259.
[23] S.W. Tao, J.T.S. Irvine, Nat. Mater. 2 (2003) 320–323.
[24] S.W. Tao, J.T.S. Irvine, S.M. Plint, J. Phys. Chem. B 110 (2006) 21771–21776.
[25] J. Wan, J.H. Zhu, J.B. Goodenough, Solid State Ionics 177 (2006) 1211–1217.
[26] Q.X. Fu, F. Tietz, D. Stover, Solid State Ionics 177 (2006) 1819–1822.
[27] Z. Cheng, S.W. Zha, L. Aguilar, D. Wang, J. Winnick, M.L. Liu, Electrochem. Solid State Lett. 9 (2006) A31–A33.
[28] A.L. Sauvet, J. Fouletier, F. Gaillard, M. Primet, J. Catal. 209 (2002) 25.
[29] T. Nakamura, G. Petzow, L.J. Gauckler, Mater. Res. Bull. 14 (1979) 649.
[30] H. Yokokawa, N. Sakai, T. Kawada, M. Dokiya, Solid State Ionics 52 (1992) 43.
[31] J. Sfeir, J. Power Sources 118 (2003) 276–285.
[32] A.L. Sauvet, J.T.S. Irvine, Solid State Ionics 167 (2004) 1–8.
[33] J. Pena-Martinez, D. Marrero-Lopez, J.C. Ruiz-Morales, C. Savaniu, P. Nunez, J.T.S. Irvine, Chem. Mater. 18 (2006) 1001–1006.
[34] S.W. Tao, J.T.S. Irvine, J.A. Kilner, Adv. Mater. 17 (2005) 1734–1737.
[35] H.P. He, J.M. Hill, Appl. Catal. A 317 (2007) 284–292.
[36] N. Yamazoe, Y. Teraoka, Catal. Today 8 (1990) 175.
[37] R.H.E. van Doorn, H. Kruidhof, A. Nijmeier, A.J.A. Winnubst, A.J. Burggraaf, J. Mater. Chem. (1998) 2109–2112.
[38] A. Vogel, Textbook of Quantitative Inorganic Analysis, Longman, Harlow, England, 1986.
[39] A.C. Larson, R.B. Von Dreele, General Structure Analysis System (GSAS), Los Alamos National Laboratory Report LAUR86-748, 2000, pp. 1–221.
[40] Y.H. Hu, E. Ruckenstein, in: B.C. Gates, H. Knözinger (Eds.), Advances in Catalysis, vol. 48, pp. 297–345.
[41] N. Laosiripojana, S. Assabumrungrat, Appl. Catal. B 60 (2005) 107.
[42] M.C.J. Bradford, M.A. Vannice, Catal. Rev. 41 (1999) 1–42.
[43] M. Valkeapaa, S. Eriksson, R. Mathieu, P. Svedlindh, J. Eriksen, H. Rundlof, Ferroelectrics 270 (2002) 1297–1302.
[44] S. Estemirova, A. Fetisov, V. Balakirev, S. Titova, J. Supercond. Novel Magnetism 20 (2007) 113–116.
[45] Y.J. Yang, T.L. Wen, H.Y. Tu, D.Q. Wang, J.H. Yang, Solid State Ionics 135 (2000) 475–479.
[46] K. Rida, A. Benabbas, F. Bouremmad, M.A. Pena, A. Martinez-Arias, Catal. Commun. 7 (2006) 963–968.
[47] S.W. Zha, P. Tsang, Z. Cheng, M.L. Liu, J. Solid State Chem. 178 (2005) 1844–1850.
[48] H. Fukunaga, M. Ihara, K. Sakaki, K. Yamada, Solid State Ionics 86 (8) (1996) 1179–1185.